

# Chapter 12

## Metrologies for Mechanical Response of Micro- and Nanoscale Systems

Robert R. Keller, Donna C. Hurley, David T. Read, and Paul Rice

### 12.1 Introduction

Thin films and nanomaterials lie at the heart of the burgeoning fields of nano-electronics and nanotechnology, and the accurate measurement of their properties provides a basis for consistent manufacturing, fair trade, and reliable performance. Introduction of such materials into current and future technologies has opened an entirely new suite of both materials science and measurement science challenges – effects of dimensional scaling play a stronger role in the reliability of thin films and nanomaterials than in any other materials previously known. Surfaces and interfaces can dominate and change behaviors and properties known to develop in bulk materials of the same chemical composition. As a result, extrapolation of bulk responses to the nanoscale is often inaccurate.

This chapter describes metrologies developed by NIST scientists and collaborators for mechanical properties of dimensionally constrained materials; these approaches make use of methods inherently sensitive to small volumes. Attention is focused on emerging test methods for several key forms of mechanical response – elasticity, strength, and fatigue. We attempt to avoid excessive duplication of discussion contained in other chapters. Emphasis is placed on structures that are volume constrained, with one or more dimensions less than 1  $\mu\text{m}$  and often less than 100 nm.

The first metrology is contact-resonance atomic force microscopy (AFM), wherein the mechanical resonance properties of an AFM cantilever in contact with a thin-film or nanoparticle-based specimen are shown to depend sensitively on the elastic properties of a small volume of material beneath the tip. The second metrology is microtensile testing, wherein thin-film specimens are patterned into

---

R.R. Keller, D.C. Hurley, D.T. Read, and P. Rice  
National Institute of Standards and Technology, Materials Reliability Division, Boulder, CO 80305  
keller@boulder.nist.gov, hurley@boulder.nist.gov, read@boulder.nist.gov,  
paul.rice@colorado.edu

free-standing tensile specimens by use of integrated circuit fabrication methods, and force–displacement response measured. The third metrology is based on application of controlled Joule heating to patterned thin films on substrates by alternating current, for the purpose of measuring fatigue and strength of thin patterned films on substrates.

## 12.2 Contact-Resonance AFM Methods for Nanoscale Mechanical Properties

Many emerging nanotechnology applications require nanoscale spatial resolution in more than one dimension. Furthermore, in many new applications it is desirable to visualize the spatial distribution in properties. This is because new systems increasingly involve several disparate materials integrated on the micro- or nanoscale (e.g., electronic interconnect, nanocomposites). Failure in such heterogeneous systems frequently occurs due to a localized variation or divergence in properties (void formation, fracture, etc.). Engineering these complex systems therefore requires quantitative nanomechanical imaging to better predict reliability and performance.

Methods utilizing the atomic force microscope (AFM) [1] present an attractive solution for characterizing mechanical properties with true nanoscale resolution. The AFM's scanning capabilities and the small radius of the cantilever tip (typically 5–50 nm) enable rapid, in situ imaging with nanoscale spatial resolution. The AFM was originally created to measure surface topography with atomic spatial resolution [1]. Since then, several AFM techniques to sense mechanical properties have been demonstrated [2–6]. For relatively stiff materials such as ceramics or metals, the most promising AFM methods for quantitative measurements are dynamic approaches, in which the cantilever is vibrated at or near its resonant frequencies [7]. These methods are often called “acoustic” or “ultrasonic” due to the frequency of vibration involved ( $\sim 100\text{kHz} - 3\text{MHz}$ ). Among them are ultrasonic force microscopy (UFM) [8], heterodyne force microscopy [9], ultrasonic atomic force microscopy (UAFM) [10], and atomic force acoustic microscopy (AFAM) [11]. A general name for all of these approaches is “contact-resonance-spectroscopy AFM” or simply “contact-resonance AFM.”

Of these methods, AFAM has arguably achieved the most progress in quantitative measurements. In this section, we describe how contact-resonance AFM methods can be used for quantitative measurements and imaging of nanoscale mechanical properties. We present the basic physical concepts, and then explain how they can be used to measure elastic properties. Techniques are described to obtain measurements at a single sample position as well as by both qualitative and quantitative imaging. Results are shown for specific material systems in order to demonstrate the potential of the techniques for nanoscale materials characterization.

### 12.2.1 Principles of Contact-Resonance AFM

Contact-resonance AFM methods make use of resonant modes of the AFM cantilever in order to evaluate near-surface mechanical properties. Several groups have developed approaches based on the basic principles described here [11–16]. Resonant vibrational modes of the cantilever are excited by either a piezoelectric element attached to the AFM cantilever holder or an external actuator such as an ultrasonic transducer. Typically, the two lowest-order flexural (bending) modes of the cantilever are used. When the tip of the cantilever is in free space, the resonant modes occur at the free or natural frequencies of the cantilever. The exact values of the resonant frequencies are determined by the geometry and material properties of the cantilever. When the tip is brought into contact with a specimen by applying a static load, the frequencies of the resonant modes are higher than the corresponding free-space values, due to tip–sample forces that stiffen the system. Contact-resonance AFM methods involve exciting these “free-space” and “contact-resonance” modes, and measuring the frequencies at which they occur. The frequency data are then interpreted with appropriate models in order to deduce the mechanical properties of the sample.

After acquiring contact-resonance spectra in the manner described below, the frequency information is first analyzed with a model for the dynamics of the vibrating cantilever. Both analytical [15, 17] and finite-element [14, 18] analysis approaches have been used. The simplest model to describe the interaction is shown in Fig. 12.1a. The cantilever is modeled as a rectangular beam of length  $L$  and stiffness  $k_c$  (spring constant). The cantilever is clamped at one end. It is coupled to the sample by a tip located a distance  $L_1 < L$  from the clamped end. The coupling between the tip and sample is assumed to be purely elastic and is therefore represented by a spring of stiffness  $k$ . This assumption is valid if the applied load  $F_N$

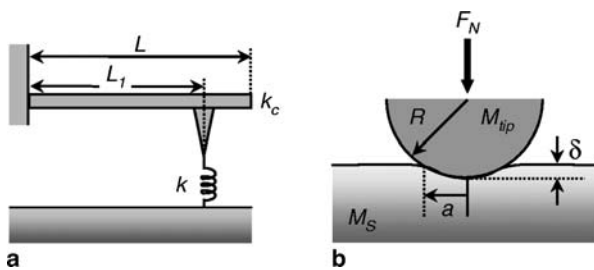


**Fig. 12.1** Concepts of the contact-resonance AFM. **(a)** Model for cantilever dynamics. A rectangular cantilever beam with stiffness  $k_c$  (spring constant) is clamped at one end and has a total length  $L$ . It is coupled to the surface through a spring of stiffness  $k$  (contact stiffness) located at a position  $L_1$  with respect to the clamped end. **(b)** Model for contact mechanics. A hemispherical tip of radius  $R$  is brought into contact with a flat surface under a normal applied force  $F_N$ . The resulting deformation of the surface is  $\delta$  and the radius of contact is  $a$ . The elastic properties of the tip and sample are indicated by the indentation moduli  $M_{\text{tip}}$  and  $M_s$ , respectively

is much greater than the adhesive force, but low enough to avoid plastic deformation of the sample. These conditions are valid under typical experimental conditions involving relatively stiff materials (e.g., metals, ceramics) and stiff cantilevers ( $k_c \approx 40\text{--}50 \text{ N m}^{-1}$ ), for which  $F_N \approx 0.4\text{--}2 \mu\text{N}$ .

The analytical model for cantilever dynamics provides a characteristic equation that links the measured resonant frequencies to the tip-sample contact stiffness  $k$ . If the model assumes that the AFM tip is located at the very end of the cantilever, the values of  $k$  calculated with this equation for different resonant modes are usually not equal. The adjustable tip position parameter  $L_1$  is used to ensure that the value of  $k$  is the same regardless of mode. Contact-resonance spectra are acquired for the two lowest-order flexural modes. Values of  $k$  are then calculated as a function of the relative tip position  $L_1/L$  for each mode. The value of  $L_1/L$  at which  $k$  is the same for both modes is taken as the solution. Typically,  $L_1/L \approx 0.96\text{--}0.98$ .

Elastic properties of the sample are deduced from  $k$  by means of a second model for the contact mechanics between the tip and the sample [19]. Most commonly used is Hertzian contact mechanics, which describes the elastic interaction between a hemispherical tip with a radius of curvature  $R$  and a flat surface. The parameters involved in this model are shown in Fig. 12.1b. A normal (vertical) static load  $F_N$  is applied to the tip, causing the sample to deform by an amount  $\delta$ . The contact area has radius  $a$ . The normal contact stiffness  $k$  between the tip and the sample is given by

$$k = 2aE^* = 2E^* \left[ \sqrt[3]{\frac{3RF_N}{4E^*}} \right] = \sqrt[3]{6E^{*2}RF_N}. \quad (12.1)$$

Here,  $E^*$  is a reduced modulus defined by

$$\frac{1}{E^*} = \frac{1}{M_{\text{tip}}} + \frac{1}{M_s}. \quad (12.2)$$

$M_s$  and  $M_{\text{tip}}$  correspond to the indentation (plane strain) moduli of the sample and the AFM tip, respectively. For elastically isotropic materials  $M = E/(1 - \nu^2)$ , where  $E$  is Young's modulus and  $\nu$  is Poisson's ratio. In anisotropic materials,  $M$  depends on direction and is calculated from the second-order elastic stiffness tensor [20].

In principle, one could measure  $a$  directly, or determine  $R$  and  $F_N$  for a given experiment and calculate  $a$ . Equation (12.1) could then be used to determine  $E^*$ , from which the modulus  $M_s$  could be found using (12.2). This approach is difficult in practice. With typical values of  $R = 25 \text{ nm}$ ,  $F_N = 1 \mu\text{N}$ , and  $E^* = 80 \text{ GPa}$ , (12.1) yields  $a \approx 6 \text{ nm}$ . Although the small size of  $a$  is precisely why contact-resonance AFM methods can achieve nanoscale spatial resolution, it means that direct measurements of  $a$  are very difficult. To overcome this problem, the referencing approach described below has been developed for use in experiments [15, 21].

### 12.2.2 Modulus Measurements

Contact-resonance AFM experiments are performed with an apparatus such as the one shown schematically in Fig. 12.2a. The apparatus consists of a commercially available AFM and a few off-the-shelf components. The specimen is bonded to an ultrasonic piezoelectric transducer mounted on the AFM translation stage. The transducer is excited with a continuous sine wave voltage by a function generator. The amplitude of the cantilever deflection is monitored by the AFM’s internal position-sensitive photodiode. Lock-in techniques are used to isolate the component

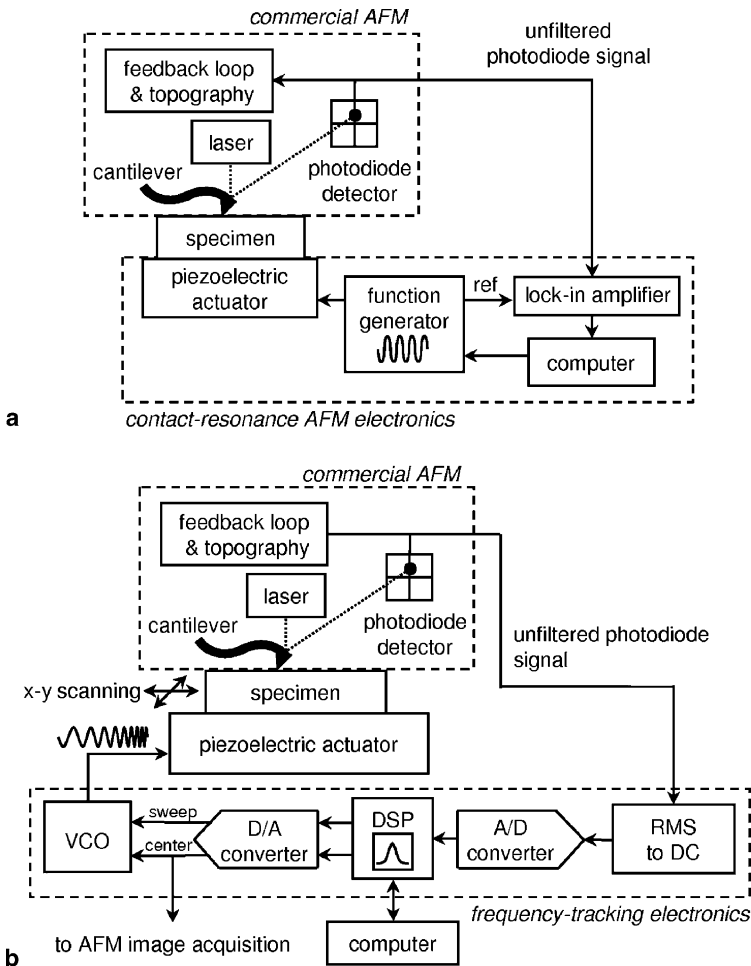


**Fig. 12.2** Schematics of experimental apparatus used in the contact-resonance AFM experiments. (a) Apparatus for modulus measurements at a fixed sample or for qualitative imaging. (b) Frequency-tracking apparatus for quantitative imaging

of the photodiode signal at the excitation frequency. In this way, a spectrum of the cantilever response vs. frequency can be obtained by sweeping the transducer excitation frequency and recording the lock-in output signal. The typical frequency range involved ( $\sim 0.1\text{--}3\text{ MHz}$ ) means that it is necessary to have access to the unfiltered photodiode output signal from the AFM.

Contact-resonance spectra are acquired for transducer excitation voltages low enough to ensure a linear interaction, i.e., the tip remains in contact with the sample at all times. As described above, spectra for two different resonant modes are used to determine the correct value of  $k$  and the tip position  $L_1/L$ . Resonance frequency is measured on two samples in alternation: (1) the test or unknown sample, and (2) a reference or calibration specimen whose elastic properties have been determined by another means. The measured contact-resonance frequencies are used to calculate values of  $k$  for both the test and reference materials with the cantilever-dynamics model described above.

If measurements are performed on the test (subscript  $s$ ) and reference (subscript  $\text{ref}$ ) samples at the same values of  $F_N$ , it can be shown [21] that

$$E_s^* = E_{\text{ref}}^* \left( \frac{k_s}{k_{\text{ref}}} \right)^m, \quad (12.3)$$

where  $m = 3/2$  for Hertzian contact and  $m = 1$  for a flat punch. The indentation modulus  $M_s$  of the test sample is then determined from  $E_s^*$  by use of (12.2) and knowledge of  $M_{\text{tip}}$ . Because the true shape of the tip is usually intermediate between a hemisphere and a flat [22], the values calculated with  $m = 3/2$  and  $m = 1$  set upper and lower limits on  $M$ , respectively. Multiple data sets are obtained by comparing measurements on the unknown sample to those made on the reference sample immediately before and afterward. Averaging the data sets yields a single value for the indentation modulus  $M_s$  of the test sample.

The referencing approach eliminates the need for precise knowledge of  $R$ ,  $F_N$ , and  $a$  (see (12.1)), which are difficult to determine accurately. Because  $k$  depends on the contact area, this approach assumes that the contact geometries for the test material and for the reference material are identical. An alternative approach that avoids this assumption by means of a tip-shape-estimation procedure has also been developed [23]. Accuracy may also be improved by use of multiple reference samples [14, 24, 25].

The accuracy of this technique has been examined experimentally by comparing contact-resonance measurements with values obtained by other methods [14, 26]. Some example results are shown in Fig. 12.3. Values for the indentation modulus  $M$  were obtained for several thin supported films of different materials by means of contact-resonance AFM (AFAM), nanoindentation (NI), and surface acoustic wave spectroscopy (SAWS). NI is destructive to the sample and has somewhat poorer spatial resolution than AFM methods, but is widely used in industry. The SAWS method is nondestructive and is used primarily in research laboratories. The values obtained by SAWS represent the average properties over a few square centimeters

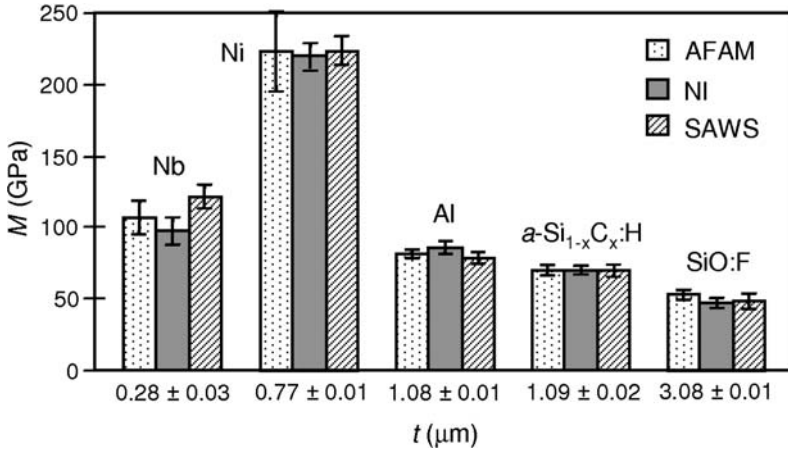


**Fig. 12.3** Indentation modulus  $M$  of thin supported films obtained by contact-resonance AFM (AFAM), nanoindentation (NI), and surface acoustic wave spectroscopy (SAWS). The thickness  $t$  of each film was determined by cross-sectional SEM analysis or by stylus profilometer methods. Film materials include fluorinated silica glass (FSG), amorphous hydrogenated silicon carbide ( $a\text{-Si}_{1-x}\text{C}_x\text{:H}$ ), aluminum (Al), niobium (Nb), and nickel (Ni). The *error bars* represent one standard deviation of the individual measurements

of the sample. It can be seen in Fig. 12.3 that the results obtained by all three methods are in very good agreement, with differences of less than 10% and within the measurement uncertainty for all of the samples.

The validity of contact-resonance AFM for elastic-property measurements having been established, it can be used to investigate specific systems. Work has spanned a wide range of materials, including piezoelectrics (PZT [27]), dickite clay [24], semiconductors (InP and GaAs [28]), and nanostructures (SnO<sub>2</sub> nanobelts [29] and ZnO nanowires [30]). A more complete survey of results can be found elsewhere [15]. Additional research is underway to better understand the range and limits of applicability of the method. For instance, how thin a film can be measured accurately without accounting for the properties of the underlying substrate? We have examined this question using a series of nanocrystalline nickel (Ni) films deposited on silicon (Si) substrates [31]. The results indicated that the modulus of films as thin as  $\sim 50$  nm could be accurately measured with contact-resonance AFM. The film thickness for which the substrate begins to play a role depends on the elastic properties of both the tip and sample. Other work has shown how to extend the basic approach described above in order to obtain further information about elastic properties [32]. By simultaneously measuring the contact-resonance frequencies of both flexural and torsional modes, shear elastic properties such as Poisson's ratio  $\nu$  or shear modulus  $G$  separately from Young's modulus  $E$ . Further work is needed to incorporate the results of these and other studies into standardized measurement procedures.

### 12.2.3 Imaging and Mapping

The scanning capabilities of the AFM mean that two-dimensional images of near-surface mechanical properties can be obtained with contact-resonance methods. Qualitative “amplitude images” indicative of local variations in stiffness are obtained with an apparatus like that in Fig. 12.2. The frequency of the excitation transducer is held constant while the tip is scanned across the sample. During scanning, the lock-in detector senses variations in the cantilever vibration amplitude at the excitation frequency due to changes in the local contact stiffness. The output signal of the lock-in is used as an external input to the AFM for image acquisition. Amplitude imaging has been used to investigate the nanoscale elastic properties of systems such as carbon-fiber-reinforced polymers [12], piezoelectric ceramics [33], and dislocations in graphite [34].

Examples of amplitude imaging are shown in Fig. 12.4. The sample contained a blanket film of an organosilicate glass (denoted SiOC) approximately 280 nm thick. Copper (Cu) lines were deposited into trenches created in the SiOC blanket film. The sample was etched briefly in a hydrofluoric acid solution in order to remove any protective surface layers. The topography image shown in Fig. 12.4a reveals that the sample is very flat, with features <10 nm high. Figure 12.4b, c shows amplitude images acquired at two different frequencies. Small features inside the Cu lines can be seen. These are most likely due to shifts in the contact area that arise from small topographical features (e.g., pores, polishing effects). In addition to the SiOC film and the Cu lines, bright regions can be seen at the SiOC/Cu interfaces. This feature corresponds to a thin barrier layer deposited on the sidewall of the trenches, and is not obvious in the topography image. In Fig. 12.4b, the SiOC regions of the image are brighter than the Cu regions. However, the Cu regions are brighter in the image in Fig. 12.4c, which was acquired at a higher excitation frequency. This information suggests that the contact-resonance frequency of the Cu regions is generally higher than that of the SiOC regions. Because higher contact-resonance frequencies imply greater elastic modulus, it can be inferred that the modulus of the Cu lines is higher than that of the SiOC film.

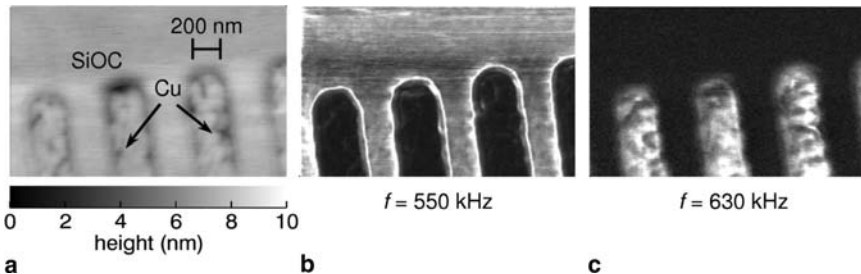


**Fig. 12.4** Example of contact-resonance AFM amplitude imaging. The sample contained copper (Cu) lines in an organosilicate glass (SiOC) film. (a) Topography. (b) Amplitude of the cantilever vibration at an excitation frequency  $f = 550$  kHz. (c) Amplitude at  $f = 630$  kHz. Images were acquired using a cantilever with lowest free-space frequency  $f_1^0 = 151.3$  kHz

Figure 12.4 shows that the components of different elastic stiffness are easily identified by amplitude imaging. However, the figure also illustrates the difficulties involved in trying to evaluate the relative stiffness of different sample components. Instead, quantitative imaging or mapping of nanoscale elastic properties is ultimately desired. Quantitative imaging involves detecting the frequency of the contact-resonance peak at each position as the tip moves across the sample. A single such contact-resonance-frequency image could provide more information than an entire series of amplitude images. However, if the sample components differ greatly in their elastic properties, the contact-resonance frequency will vary significantly across the sample making detection more difficult. Several solutions to this challenge have been demonstrated [16, 25, 26, 33, 35, 36]. Typically, there is a trade-off between the imaging speed and the amount of custom hardware and software required.

We have also developed contact-resonance-frequency imaging techniques for nanomechanical mapping [26, 37]. Our approach differs conceptually from other implementations, in that the starting frequency of the frequency sweep window is continuously adjusted to track the contact-resonance peak frequency. In this way, a high-resolution spectrum is acquired with a minimum number of data points, even if the contact-resonance frequency shifts significantly across the imaged region. Without feedback, other approaches must perform a frequency sweep at every point over the same relatively wide range that encompasses all possible peaks. Our approach also utilizes a digital signal processor (DSP) architecture. One advantage of a DSP approach is that it facilitates future upgrades, because changes are made in software instead of hardware.

A schematic of the frequency-tracking apparatus is shown in Fig. 12.2b. The circuit is described in detail elsewhere [37]. In brief, an adjustable-amplitude, swept-frequency sinusoidal voltage is applied to the piezoelectric actuator beneath the sample. As the cantilever is swept through its resonant frequency by the piezoelectric actuator, the photodiode detects the cantilever's vibration amplitude and sends this signal to the DSP circuit. Inside the circuit, the signal is converted to a voltage proportional to the root-mean-square (rms) amplitude of vibration and sent to an analog-to-digital (A/D) converter. The DSP reads the A/D converter output signal and constructs a complete resonance curve as each sweep completes. It then finds the peak in the resonance curve and uses this information in a feedback-control loop. The control loop adjusts a voltage-controlled oscillator (VCO) to tune the center frequency of vibration to maintain the cantilever response curve centered on resonance. The control voltage is also sent to an auxiliary input port of the AFM instrument for image acquisition. Each pixel in the resulting image thus contains a value proportional to the peak (resonant) frequency at that position. A frequency range can be specified in order to exclude all but the cantilever mode of interest. A total of 128 data points are acquired for each resonance curve, and at  $48 \text{ kS s}^{-1}$  the system is capable of acquiring the full cantilever resonance curve 375 times per second. The currently implemented circuit realizes approximately 17–18 bits of resolution, corresponding to a frequency resolution of about 12 Hz over the full-range span of 3 kHz–3 MHz. The AFM scan speed must be adjusted to ensure that

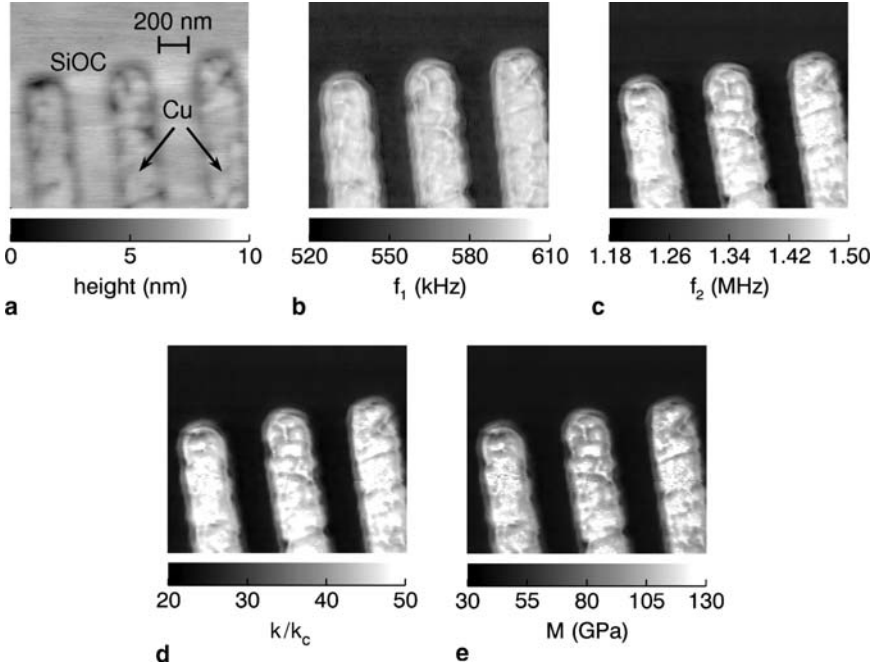


**Fig. 12.5** Example of quantitative contact-resonance AFM imaging. The images correspond to approximately the same region of the SiOC/Cu sample shown in Fig. 12.4. Contact-resonance-frequency images of (a) first ( $f_1$ ) and (b) second ( $f_2$ ) flexural modes, respectively. (c) Normalized contact stiffness  $k/k_c$  calculated from (a) and (b). (d) Map of the indentation modulus  $M$  calculated from (c) assuming flat-punch contact mechanics. The free-space frequencies of the cantilever's lowest two flexural modes were  $f_1^0 = 151.3$  kHz and  $f_2^0 = 938.0$  kHz

several spectrum sweeps are made at each image position. For scan lengths up to several micrometers, an image with  $256 \times 256$  pixels is usually acquired in less than 25 min.

An example of quantitative imaging with our frequency-tracking electronics is shown in Fig. 12.5. The images correspond to the same region of the SiOC/Cu structure in Fig. 12.4. The topography image in Fig. 12.5a shows the SiOC blanket film and the slightly recessed ( $<5$  nm) Cu lines. The contact-resonance-frequency images for the two lowest flexural modes of the cantilever are shown in Fig. 12.5b, c, respectively. The frequency images reveal directly that the contact-resonance frequency in the Cu regions is higher than in the SiOC regions.

An image of the normalized contact stiffness  $k/k_c$  calculated from the images of  $f_1$  and  $f_2$  is shown in Fig. 12.5d. The image was calculated on a pixel-by-pixel basis with the analysis approach described above for point measurements. Depending on the sample and type of information desired, it may be sufficient to evaluate the contact-stiffness map alone. In other cases, it may be preferable to calculate a map of the indentation modulus  $M$  from the contact-stiffness image. Such calculations involve the same models and assumptions used in point measurements of  $M$ . For instance, it is necessary to choose a specific contact-mechanics model, and to

assume that the model remains valid for the entire image (i.e., tip wear is not dramatic). Reference values of  $E^*$  and  $k/k_c$  are also needed. Here, we calculated a map of the indentation modulus  $M$  from the contact-stiffness image assuming that the tip was flat. We assumed that the mean value of  $E^*$  for the SiOC region corresponded to  $M_{\text{SiOC}} = 44.3 \text{ GPa}$ . This value was obtained from point measurements made directly on the SiOC film. For the reference value of  $k/k_{\text{lever}}$ , we used the average value over the SiOC region of the image. The resulting modulus map is shown in Fig. 12.5e. Although some assumptions were made to obtain the map, it shows that quantitative values for  $M$  can be achieved.

Other mechanical properties besides elastic modulus can be imaged with contact-resonance AFM methods, if they influence the contact stiffness between the tip and the sample. One such property of technological interest is the relative bonding or adhesion between a film and a substrate. To experimentally investigate the sensitivity of contact-resonance AFM to variations in film adhesion [38], we fabricated a model system of gold (Au) and titanium (Ti) films on (001) silicon (Si). Figure 12.6a shows a cross-sectional schematic of the sample. A rectangular grid with  $5 \mu\text{m} \times 5 \mu\text{m}$  squares (10- $\mu\text{m}$  pitch) of Ti was created on Si by standard micro-fabrication techniques. A blanket film of gold (Au) and a 1-nm topcoat of Ti were deposited on top of the grid. The sample was intended to contain variations in the adhesion of a buried interface, but only minimal variations in topography and composition at the surface. A crude scratch test was performed by lightly dragging one end of a tweezer across the sample. Optical micrographs showed that this treatment had removed the film in the scratched regions without a Ti interlayer (squares), but left the gold intact in the scratched regions containing a Ti interlayer (grid). The result confirmed our expectation that the film adhesion was much stronger in regions containing the Ti interlayer. The Ti topcoat was included merely to prevent contamination of the AFM tip by the soft Au film.

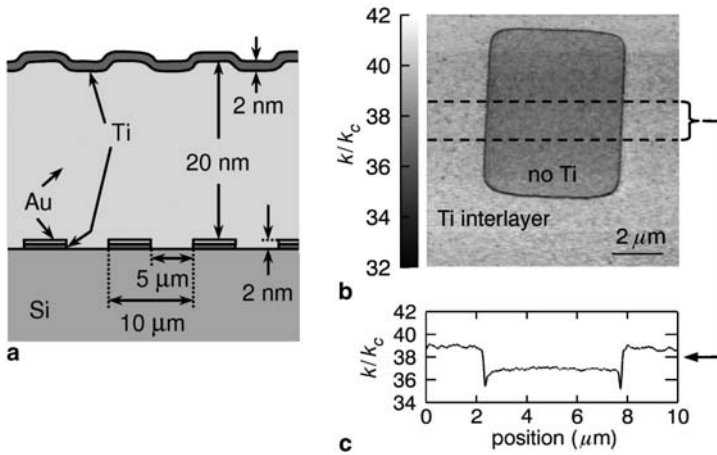


**Fig. 12.6** Imaging of film/substrate adhesion. (a) Schematic of sample in cross section. (b) Map of the normalized contact stiffness  $k/k_c$  calculated from contact-resonance-frequency images. (c) Average stiffness vs. position across the center of (b)

To understand how contact-resonance methods sense variations in a buried interface, note that experiments probe the sample properties to a depth  $z \approx 3a$ , where  $a$  is the tip-sample contact radius [19]. For Hertzian contact mechanics,  $a^3 = (3RF_N)/(4E^*)$ . For  $z > 3a$ , the stress field beneath the tip is sufficiently small relative to its value at the surface (less than 10%) that the measurement is not sensitive to property variations. The relative depth sensitivity of contact methods is determined by the choice of experimental parameters  $R$  and  $F_N$ , as well as the sample and tip properties ( $E^*$ ). We estimate that  $a = 6\text{--}8.5$  nm for our experimental conditions. Therefore, the experiments should probe the film interface ( $z = 22\text{--}24$  nm  $\approx 3a$ ).

Contact-resonance-frequency imaging experiments were performed on the sample with the methods described above. An image of the normalized contact stiffness  $k/k_c$  calculated from the experimental contact-resonance-frequency images of  $f_1$  and  $f_2$  is shown in Fig. 12.6b. The image reveals that the contact stiffness is lower in the square region with poor adhesion (no Ti interlayer). A line scan of the average value of  $k/k_c$  vs. position obtained from 40 lines in the center of the image is shown in Fig. 12.6c. The mean value of  $k/k_c$  is  $39.1 \pm 0.6$  in the grid regions and  $37.1 \pm 0.5$  in the square, a difference of 5%. Several other contact-stiffness images acquired at different sample positions consistently showed a decrease in  $k/k_c$  of 4–5% for the regions of poor adhesion that lacked a Ti interlayer.

The results are consistent with theoretical predictions for layered systems with disbonds [39]. An impedance-radiation theory was used to model the disbonded substrate/film interface by a change in boundary conditions (i.e., zero shear stress at the interface). For a disbond in a 20 nm aluminum film ( $M = 78$  GPa) on (001) Si ( $M = 165$  GPa), a reduction of approximately 4% in the contact stiffness was predicted, very similar to our results. The system modeled in Ref. [39] contained a film material different from that used in our experiments. However, the overall combination of conditions (film and substrate modulus, applied force, etc.) was sufficiently similar to ours that we believe a comparison is valid. These results represent progress toward quantitative imaging of adhesion, a goal with important implications for the development of thin-film devices in many technological applications.

## 12.3 Microtensile Testing

Techniques for microtensile testing of thin films have now been under development at NIST Boulder for over 10 years [40–42]. This section reviews and summarizes the rationale behind microtensile testing, and the current state of the experimental techniques available here. Only experimental techniques in use at the authors' laboratory are described in detail; many alternative techniques for obtaining information about the strength, ductility, and other mechanical properties of micro- and nanoscale materials are being explored elsewhere. An extensive list of microtensile results from the literature is given, to emphasize the usefulness of the microtensile technique.

### ***12.3.1 Rationale for Microtensile Testing***

Tensile testing is the standard means of obtaining mechanical properties of structural metals [43]. Because the stress field is uniaxial and uniform throughout the gage section until significant plastic strain occurs, unambiguous and accurate Young's modulus, yield strength, ultimate tensile strength, and ductility can be obtained from an accurate force–displacement record. For macroscale structures, these properties are often specified for a given material and used for comparison of alternative materials, development of new materials, and quality control. In addition, tensile properties are the essential input parameters for structural design and numerical modeling and simulation of mechanical behavior of structures. These modeling and simulation techniques are routinely applied to micro- and nanoscale structures used in advanced microelectronics devices and are a fundamental tool in designing applications of nanomaterials. The accuracy of the results of these analytical efforts depends on the accuracy of the material property values used as input. However, it has long been realized that micro- and nanometer-sized thin films typically have microstructures and properties, produced by their fabrication processes, that are different from the microstructures and properties of bulk materials of the same nominal chemical composition [44,45]. Usefully accurate estimates of properties of films prepared by one process often cannot be made from films prepared by another process or from bulk specimens. The properties of thin films need to be measured in the dimension and conditions that are used in actual structural applications. Therefore, accurate methods for mechanical characterization of micro- and nanoscale materials are needed, and tensile testing is being developed to meet this need. Tensile test techniques applicable to micro- and nanoscale materials are only now beginning to be used as part of the commercial design and quality control of advanced small-scale devices and structures.

### ***12.3.2 Specialized Techniques Required***

Tensile properties of macroscale materials are generally measured according to standardized procedures, such as ASTM E8 and ASTM E345 [46,47]. Specimens specified in these test methods are typically several millimeters or even centimeters in thickness for rectangular specimens (or in diameter for round specimens); these dimensions are orders of magnitude larger than thin films used in today's microelectronics industry. The testing machines, gripping devices, and specimen-preparation procedures prescribed in the standard test methods are difficult to apply in testing thin films that have thicknesses measured in micro- or nanometers. Early developments of the experimental techniques have been reviewed by Hoffman [48] and Menter and Pashley [49]. Most of the specimens used in these early approaches were still relatively large compared with those of current interest. Early attempts to pull thin films in conventional testing machines used specimens lifted from the substrate; researchers encountered problems in placing the specimen on the grips

without excessive wrinkling, and depended on special separation layers beneath the specimen film, such as water soluble sodium chloride. Specimen fabrication, preparation, and especially mounting specimens to the loading devices were cited as major difficulties.

### ***12.3.3 Bulk Micromachined Microtensile Specimens***

The test methods for thin films, at NIST and elsewhere, took a big step forward with the introduction of microfabrication techniques, including lithography, deposition, and etching, to produce tensile specimens [40, 50–53]. Microfabrication of tensile specimens brought its own advantage, namely, that a large number of specimens with uniform thickness, composition, geometry, and structure are fabricated in a single process run. It became evident that since films in actual devices are always produced on substrates, the use of the substrate to support the thin film specimen is appropriate. Bulk micromachining of MEMS devices had been developed by this time, demonstrating the concept of etching away a selected portion of the original substrate to form a useful device. But the substrate is always much more massive than the film, so it must be removed at least from beneath the gage section of the specimen. The fabrication challenge here is the chemical selectivity required to etch through hundreds of micrometers of silicon without damaging the metal specimen. Aqueous hydrazine has been used, but this material is hazardous. Another disadvantage is the large width of the gage section, 100  $\mu\text{m}$  or more, compared to the line widths used in microelectronic interconnect structures and also compared to a typical film thicknesses of 1  $\mu\text{m}$ . Ding et al. [50] reported the use of a silicon frame design for testing doped silicon. The first realization of this scheme for metal films was the silicon frame tensile specimen [40]. To produce the silicon frame tensile specimen, photolithographic patterning is used to form a straight and relatively narrow gage section with larger grip sections on a silicon frame. The substrate beneath the gage section is removed by a suitable etchant. The silicon frame, carrying its tensile specimen of a thin film, is mounted on a suitable test device capable of supplying force and displacement [54]. The silicon frame is cut, while leaving the specimen undamaged. This step has been accomplished manually with a dental drill, using a temporary clamp to hold the specimen in place, and by the use of a cutting wheel mounted on a moveable stage [53]. A device driven by piezoelectric blocks was used to conduct tensile and fatigue tests on aluminum and copper films using the silicon frame tensile specimen [54–56]. Similar specimens and instrumentation have been used at other laboratories.

All the microtensile (MT) techniques include measurements of force and displacement. The force is measured using a load cell, either commercial or custom-built. For the generation of bulk-micromachined specimens discussed so far, the force might amount to 0.1 N; commercial load cells with this range are available. The challenge in displacement measurement for microscale testing is the same in

principle as for macroscale testing: Measurement of the stretch of the gage section, which may be much different from the displacement of the load fixture because of the variable compliance of the load train. But the adaptation of common macroscale techniques for measurement of strain in a thin film proved impossible. Adhesively bonded strain gages or displacement gages clipped onto the specimen have not been successfully scaled down to dimensions useful for testing of thin films. Optical techniques have been adapted instead. Displacement has been measured by interferometric techniques such as electron speckle pattern interferometry (ESPI), for example as in [57], or by diffraction from markers placed on the specimen surface [58].

### 12.3.4 Surface-Micromachined Tensile Specimens

In recent years, a new generation of smaller-scale tensile specimens produced by surface micromachining and complementary test techniques, has been developed [41, 59, 60]. The NIST-Boulder version is described here. Depending on the material to be tested and the deposition processes used, the pattern-and-etch steps may vary. The substrates used originally were (100) silicon wafers coated by suppliers with a “wet” oxide layer about  $0.5\ \mu\text{m}$  thick. A typical fabricated specimen ready for testing is shown in Fig. 12.7. A mask-pattern-etch procedure was used to produce a rectangular window in the oxide, exposing the underlying bare silicon where the specimen would be formed. More recently, entirely uncoated silicon wafers have

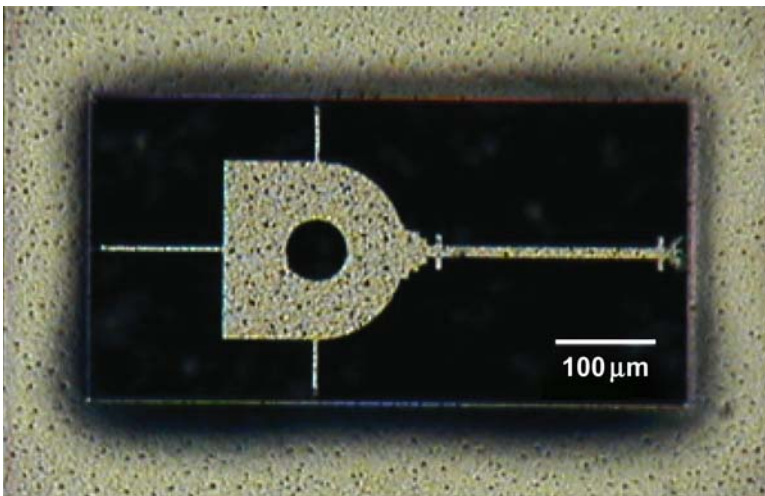


**Fig. 12.7** Fabricated microtensile specimen ready for testing. The gage section, which is the long section to the right of the structure, is just under  $200\text{-}\mu\text{m}$  long. The *hole*, which is used for loading, is about  $50\ \mu\text{m}$  in diameter. The *narrower lines* connected to the tab are the tethers, which are usually cut before testing

been used. This eliminated a processing step. The specimen material is deposited as a blanket film, aluminum in Fig. 12.7. The specimen geometry is formed, within the region of exposed silicon on oxidized wafers or at arbitrary locations on bare wafers, by subtractive photolithography using masking and wet-chemical etching. One end of the specimen's gauge section (right side in Fig. 12.7) connects to the surrounding film that remains adhered to the oxidized silicon. The other end connects to a tab, which has a hole of  $50\mu\text{m}$  in diameter for pin-loading. There are three tethers connected to the tab, as shown in Fig. 12.7. The function of the tethers is to hold the tab in place after the underlying silicon has been removed. More recent designs have eliminated some of the tethers. The gauge section, the tab, and the tethers are freed by chemically removing the underlying silicon substrate with xenon difluoride ( $\text{XeF}_2$ ). This dry etchant very selectively attacks silicon, but is stopped by  $\text{SiO}_2$ , copper, aluminum, polyimide, and many other materials of interest in the electronics industry. For easy loading, the silicon needs to be removed to a depth of at least  $50\mu\text{m}$  everywhere within the rectangular etch region.

The original design [61] for the loading hole was a square because it was more convenient for the mask-design software to generate. During testing, however, failure commonly occurred at the loading hole with cracks initiated at the corners of the hole. The current specimen has a circular hole that eliminates the loading-hole failure in thick specimens, while loading-hole reinforcement through selective lithography is also used in specimens made from thinner films. At the ends of the gauge section, there are flags that facilitate the measurements of displacement and strain by the digital image correlation technique [62, 63]. The nominal dimensions for the gauge section of the rectangular specimen are  $180\mu\text{m} \times 10\mu\text{m} \times 1\mu\text{m}$ . Variants with thickness down to  $0.5\mu\text{m}$  and up to  $10\mu\text{m}$  have been tested. For stress and strain calculations, the dimensions of each specimen are individually measured. The thickness is determined by a profilometer. The length and width are measured with a scanning electron microscope (SEM). The measurement accuracy of length and width is within  $\pm 1\%$ , while thickness is within  $\pm 3\%$ .

### ***12.3.5 Microtensile Apparatus***

Our present test apparatus consists of the following components:

1. A three-axis micromanipulator, which is assembled from three separate commercial single-axis stages, each driven by an inchworm piezomotor. The motors are controlled by a desktop computer with a specialized interface and software. According to the manufacturer, each axis of the micromanipulator assembly has a travel range of 25 mm. The motor drive for each axis has an encoder with a resolution of  $0.05\mu\text{m}$ . We move the manipulator by specifying end points, but the displacement rates vary from the nominal values because of the variable action of the piezo-stepping of the motors. The motors have a nominal speed range from  $0.004$  to  $1,000\mu\text{m s}^{-1}$ . It is noted that the manufacturer's specifications of

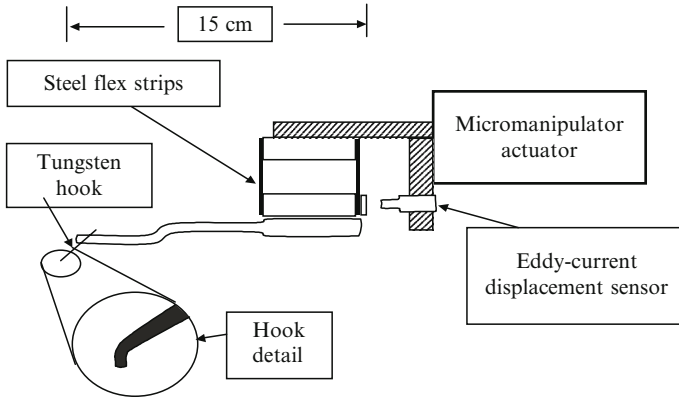


**Fig. 12.8** Schematic drawing of a loading system with tungsten loading pin or hook mounted at the end of the brass rod and force sensor assembly

the micromanipulators given here are for reference only. The actual strains of a specimen during a test are determined from digital images of the specimen surface.

2. A loading system consisting of tungsten pin, brass rod, and force sensor, which is carried by the micromanipulator assembly, as shown in Fig. 12.8. The force sensor contains an eddy-current displacement sensor and two spring steel flex strips. As shown in the figure, the ends of the steel strips are screw-fastened to two ceramic blocks that serve as a heat insulator when tests are performed at elevated temperatures. The top ceramic block is attached to the micromanipulator assembly and the bottom one is supported by the flex strips. The brass loading rod with the tungsten pin at its end is attached to the bottom ceramic block. The rod is aligned to one of the micromanipulator's axes to facilitate alignment during testing. The sharp tungsten pins are commercially available as electrical contacts for wafer probes. We bend the tip  $45^\circ$  so it will be normal to the surface of the specimen, and blunt it to a diameter of about  $40\mu\text{m}$  to fit the hole in the specimen's tab. The steel flex strips have a fixed nominal length of 20.3 mm and a width of 6.4 mm. Two thicknesses, 0.13 mm and 0.38 mm, have been used depending on the force required. The eddy-current sensor monitors the deflection of the lower ceramic block against the stiffness of the flex strips. With the 0.13-mm plates, the sensitivity is about 8 mN for the nominal range of the eddy current sensor, which is  $25\mu\text{m}$ . For the 0.38-mm plates, the sensitivity is about 150 mN for the same deflection range.
3. An optical microscope equipped with a digital camera. High magnification is needed to view the specimen for alignment and for engagement of the loading pin to the specimen under manual control of the micromanipulator. The images of the specimen surface during the course of a test are required for calculation of specimen's extensions and strains. We use a simple  $25\times$  objective lens with a working distance of about 20 mm to view the specimen while we engage the

loading pin; then we move the microscope to view and record images of the specimen gage during the test. The 200- $\mu\text{m}$  gage length of the specimen was chosen to nearly fill the field of view of the digital camera on the microscope. The long working distance is needed to leave room for the loading system between the lens and the surface of the specimen. We also have conducted tests in the SEM, which has continuous magnifications that provide sufficient flexibility for handling and testing specimens. However, the time required to pump down the SEM and its slower image acquisition has led us to prefer the optical microscope for microscale testing.

4. A second desktop computer controls a digital camera on the microscope to acquire images of the specimen surface during testing. The two computers are synchronized through communications via serial ports on the computers, so that the individual data points for force and stage movement can be associated with the proper corresponding image. Our camera acquires grayscale images of  $1,280 \times 1,024$  pixels, although we save only  $1,280 \times 256$  pixels.

### ***12.3.6 Force Calibration***

While force calibrations for conventional mechanical test machines are based on dead weights and gravity, dead-weight calibration with standard gram-denominated masses is not practical for the load cells used in present-day microtensile testing. For example, an aluminum specimen of the nominal  $1 \times 10 \mu\text{m}^{-2}$  cross section fails at an applied load of approximately 2 mN or less, while a mass of only 1 g provides a force of about 10 mN. Along with the minuscule forces involved is the geometry issue. Microscope stages are horizontal, so in microtensile testing the force is applied in a horizontal direction; dead-weight loads would have to be redirected from vertical to horizontal, and the needed pulleys are prone to friction. We have used a force pendulum setup for calibration. With a 20 g mass and a height of a few hundred millimeters, our setup provides on the order of 1 mN per millimeter of horizontal displacement. The friction and inertia are much less than those in simple pulley systems with comparable force levels. The setup can be trivially converted to higher force levels by using a larger mass. The accuracy of our force measurement scheme, as estimated from variability among repeat calibrations, is about 4%. For low-force measurements, the system is limited by its drift rate of about 20  $\mu\text{N}$  over times of tens of minutes. This drift is believed to be produced by temperature variation and air currents in the laboratory.

### ***12.3.7 Strain Measurement***

Our tensile testing practice typically records the engineering strain of the specimen, given by the change in length divided by the initial length. We obtain the needed

displacements of the two ends of the gage section by use of digital image correlation [62]. Our optical references for the ends of the gage section were shown in Fig. 12.7. We track the displacement of both reference shapes through the course of the test. If the specimen stays in focus, so that the images remain sharp, the precision of each position measurement is about 0.05 pixel. The gage length is about 780 pixels, so the accuracy of the strain measurement is about 60 microstrain. The range is determined by the size in pixels of the image, and is over 20% for our gage length. Digital image correlation is a powerful technique but has its pitfalls. For our system, problems have been found from “pixellation” in the cameras we have used, meaning that the individual pixels in the camera have slightly different sensitivity, so that artificial steps in intensity are introduced into the image, and from previously uncontrolled vertical motion of the specimen because of compliance in the loading system.

### 12.3.8 Our Results

Stress–strain curves obtained for thin films using the NIST apparatus are shown in Fig. 12.9, for an electrodeposited copper film [64], and Fig. 12.10, for a commercial photodefinable polyimide [65].

We often measure low modulus values, especially for electrodeposited copper [64]. On the other hand, Hurley et al. [66] showed that the values of Young’s modulus measured by a variety of test techniques, including microtensile testing, seem to be consistent.

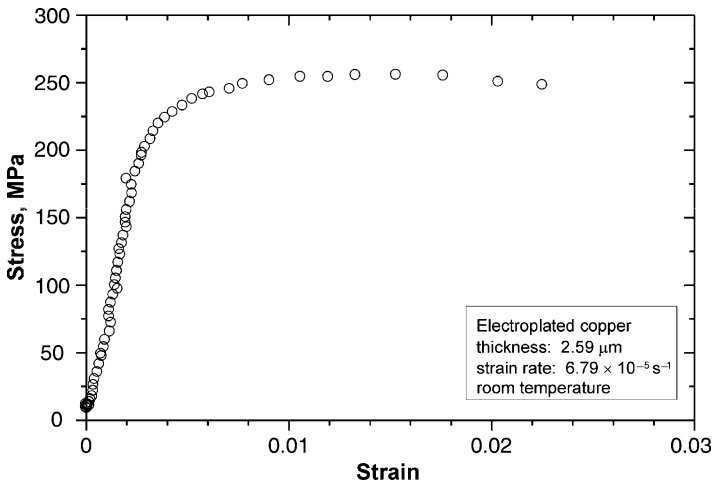


**Fig. 12.9** Stress–strain curve for an electrodeposited copper film, obtained by the NIST microtensile test technique

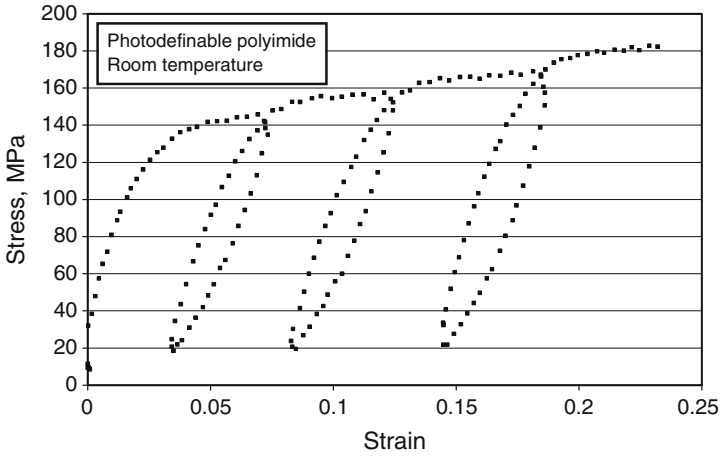


Fig. 12.10 Engineering stress–strain curve for photodefinable polyimide

### 12.3.8.1 Results in General

The underlying capability for and interest in standardization of microtensile testing is a relatively recent development. Until a few years ago, testing in one laboratory of specimens made elsewhere was a novelty. There is at present no standard test method for microtensile testing of thin films; individual investigators adapt the standard methods for bulk metal specimens to fit their specific specimen geometry. Standardization is hindered by the multitude of specimen sizes and designs that are in use, which has resulted from the difficulty of fabricating microtensile specimens. A recent round robin showed reasonable agreement among several laboratories in the strength of polySi, though most labs required their own unique specimen geometry. The different geometries were produced on the same MEMS chip [67]. The strength values obtained for polySi were impressively high, of the order of 1/30 of the polycrystalline Young’s modulus, which is the usual estimate of the theoretical strength of a solid.

### 12.3.9 Other Recent Techniques

The membrane deflection tensile test was applied to a series of face-centered-cubic (FCC) metals by Espinosa et al. [68]. Another recent advance is the cofabrication of a specimen and a protective frame that includes a force sensor [69]. This specimen is suitable for use inside a transmission electron microscope (TEM).

## 12.4 Properties of Specific Materials

Fabrication methods and test techniques for some widely used thin film materials have become sufficiently widespread so that specific values of the properties can be usefully given. Of course, Brotzen’s rule 3 still holds: the microstructure and chemical composition of the specific material at hand determine its properties. Table 12.1 shows a summary of mechanical properties for commonly used thin film materials.

**Table 12.1** Mechanical properties of selected thin films as measured by microtensile testing or nanoindentation

Material	Fabrication method	Thickness (μm)	Yield strength (MPa)	Ultimate tensile strength (MPa)	Young’s modulus (GPa)	Elongation to failure (%)	Ref.
Al	Sputtered	0.05	327		62 <sup>a</sup>		[69]
Al	Sputtered	0.1	700				[69]
Al	Sputtered	0.2	330		70		[69]
Al	e-Beam evaporated	0.2	205	375 <sup>b</sup>	65–70		[60]
Al	e-Beam evaporated	1	150		65–70		[60]
Al	e-Beam evaporated	1	94	151	24–30	22.5	[61]
Al–0.5%Cu	MOSIS <sup>c</sup>	1.5 and 2.4	65	74	40	1.4	[70]
Cu	e-Beam evaporated	0.2	345		125–129		[60]
Cu	e-Beam evaporated	1	160 <sup>d</sup>		125–129		[60]
Cu	Electrodeposited	9.7	253	311	67		[71]
Au	e-Beam evaporated	0.3, 0.5	220		53–55		[60]
Au	e-Beam evaporated	1	90		53–55		[60]
Ni	Electrodeposited	4.7		1,516	102–114		[72]
Polyimide	Spun on, baked	0.6	103	181	5.5	24	[65]
PolySi	MUMPS 25, 30 <sup>c</sup>	3.5	NA	950	157		[73]
PolySi	SUMMiT <sup>c</sup>	2.5	NA	3,000			[67]

The study by Espinosa [69] is quoted extensively here because it is recent; uses consistent methods on gold, aluminum, and copper films; includes specimen thickness and width effects; and includes considerable microstructural characterization and posttest observations of the specimens.

<sup>a</sup>The authors remark that this value shows the effect of film thickness on Young’s modulus. If correct, this would be one of the first experimental demonstrations of this theoretically predicted effect

<sup>b</sup>Unusually high value for this material and thickness

<sup>c</sup>Special proprietary deposition process; sources identified in the references

<sup>d</sup>Unusually low value for this material and thickness

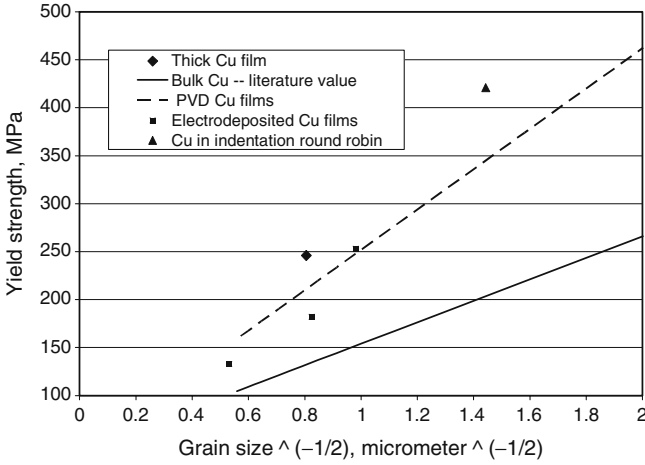


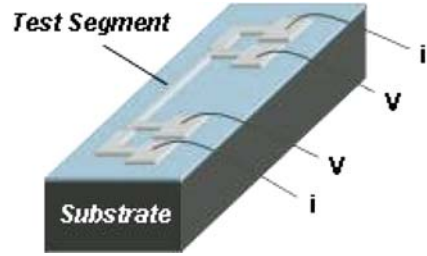
**Fig. 12.11** Yield strength of copper plotted against grain size to the minus one-half power. Bulk materials are represented as the *solid line*

It is a testament to the progress of research in thin film characterization that the large uncertainty in the mechanical properties of even 1- $\mu\text{m}$  thick films of common materials such as aluminum and copper, that existed as late as around the year 1990, is past. Now the mechanical properties of films with dimensions of 1  $\mu\text{m}$  and larger are considered to be fully understandable based on their microstructure. As an example of this, Fig. 12.11 displays the dependence of the yield strength, obtained by microtensile testing, of some copper films [74]. The yield strength values follow the trend for bulk copper. There are no “mysterious effects” arising from the *micrometer* size scale.

### 12.5 Controlled Joule Heating by Alternating Current

The microelectronics industry often makes use of thin patterned films that are not easily accessed by many of the more established methods. For example, lower-level conductors may be less than 100 nm in width, deposited into trenches, fully encased within a dielectric, and located several micrometers below the surface of a device. In order to characterize these materials with such methods, either cross sections must be prepared from fabricated devices, or special test configurations must be made, approximating the materials of interest. As a result, test specimens might not accurately represent the microstructures, geometries, or mechanical constraint conditions undergone by final products. To consider such effects, approximations and extrapolations must then be incorporated, potentially leading to considerable measurement uncertainty.

**Fig. 12.12** Schematic specimen suitable for electrical approach to fatigue and strength testing.  $V$  represents voltage probes and  $i$  represents current probes



This section introduces an alternative approach to testing the fatigue and strength properties of thin-film materials in their as-fabricated condition, by application of controlled Joule heating. This approach is applicable to systems with extremely fine dimensions, meandering geometries, multiple layers, and/or passivations. The test is based on early observations by Philofsky et al. [75], who first related alternating current loading to thermal fatigue. An electrical test method for mechanical response circumvents the need for special test configurations or specimen cross sectioning. The primary experimental requirement is that the material of interest be accessible electrically, i.e., one must be able to contact it through electrical probes or wire-bonded connections, shown schematically for a nonpassivated specimen in Fig. 12.12. Careful experimental design may allow implementation in a manufacturing environment. We discuss the principle of cyclic Joule heating as a basis for thermal fatigue testing and strength testing, and conclude with descriptions of microstructural changes induced by the test.

### 12.5.1 Cyclic Joule Heating

Application of electric current to a thin patterned film leads to Joule heating, which refers to the increase in energy of a conductor due to interactions between the conducting particles and ions making up the conductor. Alternating current applied to a conductor under conditions of low frequency and high current density can then result in cyclic Joule heating.

Mechanical testing of a patterned film on a substrate by use of AC is based on the principle that within each half cycle of current, joule heating of the current-carrying segment causes not only that segment, but also the immediately surrounding materials, to become heated. A cyclic strain,  $\Delta\varepsilon$ , results from the change in temperature,  $\Delta T$ , if there is a difference in coefficients of thermal expansion,  $\Delta\alpha$ , between the film and the substrate:

$$\Delta\varepsilon = \Delta\alpha \cdot \Delta T. \quad (12.4)$$

For the case of a film constrained by a semi-infinite substrate, nearly all of the cyclic strain is taken up by the film. Assumption of an appropriate constitutive relation such as linear elasticity then leads to a determination of cyclic stress in the film. These cyclic variables provide a means for performing fatigue tests and, as shown later, strength tests.

**Fig. 12.13** Schematic relationships between low-frequency, high-density alternating current input into a patterned metal segment and resulting temperature and mechanical stress behaviors as functions of time. Values for current density, temperature, and stress are order-of-magnitude examples

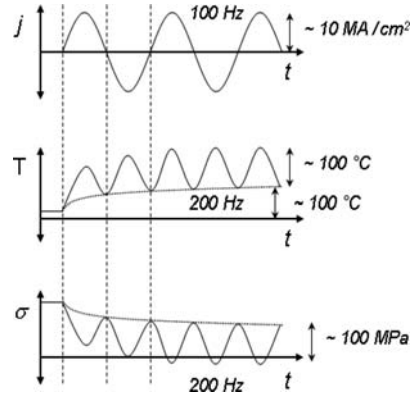


Figure 12.13 shows schematically the variations of current density,  $j$ , temperature,  $T$ , and stress,  $\sigma$ , in a patterned metal segment with time, upon exposure to an AC current. A key requirement for successful application of electrical-based tests is knowledge of specimen temperature with time. Calibration of the variation of electrical resistance,  $R$ , with temperature can be performed by measuring the (low-current) steady-state resistance of a test structure that is allowed to reach thermal equilibrium in a furnace at a variety of temperatures spanning the range of interest.

This results in  $dR/dT$  for a specific specimen material and provides a means for determining specimen temperature during the course of a test through

$$R(T) = R_0 + \Delta T \frac{dR}{dT}, \tag{12.5}$$

where  $R(T)$  is the measured specimen resistance at the unknown temperature  $T$ ,  $R_0$  is the initial room-temperature resistance, and  $\Delta T = T - T_0$ , where  $T_0$  is room temperature. Solving for  $T$  gives:

$$T = \frac{(R(T) - R_0)}{\left(\frac{dR}{dT}\right)} + T_0. \tag{12.6}$$

An example data set for the variation of temperature with time during the course of a test, as measured by resistance, is shown in Fig. 12.14, for the case of a copper line subjected to AC stressing at an RMS current density of  $17.5 \text{ MA cm}^{-2}$ , at 100 Hz. Note that it is not difficult to attain temperature amplitudes of several hundred degrees Celsius.

In order for this method to be useful as a test of mechanical response, it is important to identify the conditions that lead to well-controlled cyclic Joule heating without interference from phenomena that can affect the strain cycle, e.g., insufficient temperature cycling, or cause unintended forms of damage, e.g., electromigration.

Heat flow in materials that typically compose a microelectronic device is rapid enough to allow for nearly complete dissipation within one power cycle for frequencies up to several kilohertz [76]. Within this range of frequencies, the

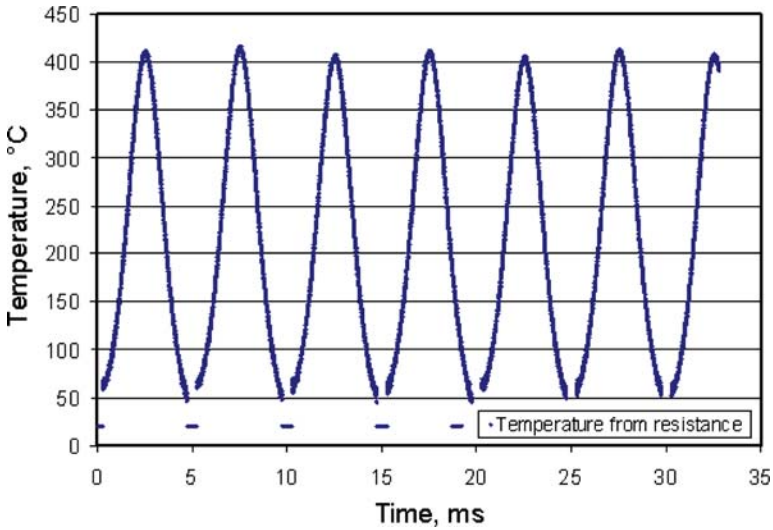


**Fig. 12.14** Example of the time-resolved variation of temperature in a patterned copper segment subjected to current stressing at  $17.5 \text{ MA cm}^{-2}$ , at an AC frequency of 100 Hz

instantaneous power varies slowly enough that steady-state conditions can be maintained throughout each power cycle. For higher frequencies, this is not the case, and it can be shown for an infinitely long, narrow line on a substrate that the temperature amplitude will decrease with the logarithm of the frequency [76]:

$$\Delta T = \frac{Q}{\pi k} (-\ln(2\omega)/2 + \text{const}), \tag{12.7}$$

where  $Q$  is the amplitude of the power per unit length,  $\omega/2\pi$  is the frequency of the electrical signal, and  $k$  is the thermal conductivity of the substrate. Practically speaking, electrical signal frequencies below several kilohertz have been found to provide sufficient temperature amplitudes for mechanical testing.

A phenomenon that could potentially induce an unintended form of damage is electromigration, where atoms of the conductor can be displaced due to momentum transfer from the conducting electrons [77]. Resulting failures take the form of voids and hillocks, which can lead to open- or short-circuit events. Electromigration damage takes place by diffusive mechanisms, suggesting the importance of time during which a stress-based driving force is active. Under conditions of AC, the important factor is the time available for diffusion during one power cycle. An estimate of diffusion distance,  $x$ , during a power cycle can be made by considering  $x = \sqrt{Dt}$ , where  $D$  is diffusivity and  $t$  is the duration of the power cycle. For lattice diffusion, a typical value of  $D$  for metallic conductors used in microelectronics is  $10^{-18} \text{ m}^2 \text{ s}^{-1}$ ; for grain boundary diffusion, a typical value of  $D$  is  $10^{-15} \text{ m}^2 \text{ s}^{-1}$ . A test running at an electrical frequency of 100 Hz, i.e., power cycling at 200 Hz, gives  $t = 0.005 \text{ s}$ , resulting in diffusion distances of 0.05 nm for lattice diffusion and

1.5 nm for grain boundary diffusion. These are relatively short distances, producing a very small amount of atomic motion in each power cycle. With a reversal in the direction of the current, most if not all of the motion may be reversed [78]. Consideration of low enough frequencies to allow nearly complete thermal dissipation in each power cycle, combined with high enough frequencies to avoid conditions that lead to electromigration damage, suggests an effective range of testing frequencies of several tens to several thousands of hertz.

### 12.5.2 Fatigue Testing

Cyclic Joule heating under properly controlled conditions provides a convenient method for performing strain-control fatigue tests on patterned materials adherent to substrates. Measurement of fatigue lifetime from a specimen entails applying constant-amplitude AC to the specimen and measuring the time to open circuit failure. Conversion to current density compensates for slight variations in cross-sectional area from specimen to specimen. Generation of a lifetime curve requires testing of multiple specimens over a range of current densities, measuring their times to failure, and plotting all data on the same graph.

Raw test data may take the form of current density plotted against lifetime, as shown in Fig. 12.15 for interconnects of copper and Al-1Si [79]. Note that the form of this data is reminiscent of S – N curves commonly found in fatigue testing of bulk materials. The data may be alternatively represented in terms of temperature amplitude, total strain amplitude, or stress amplitude vs. lifetime, through use of the resistance calibration described earlier. Replotting the data of this figure in terms of number of cycles to failure shows that the AC stressing method can be used for both low- and high-cycle fatigue measurements, with the conventional view that the transition between these regimes occurs for lifetimes in the range of  $10^4$ – $10^5$  cycles [80].

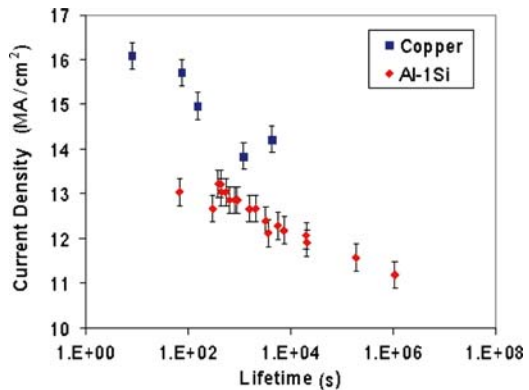


**Fig. 12.15** Fatigue lifetime plot for two types of patterned metal films on a silicon substrate. Error bars represent  $0.3 \text{ MA cm}^{-2}$  uncertainty in current density. AC electrical frequency was 100 Hz

**Table 12.2** Total strain amplitudes corresponding to various temperature ranges for the cases of aluminum on silicon ( $\Delta\alpha$  (Al/Si) =  $2.05 \times 10^{-5}$  per  $^{\circ}\text{C}$ ) and copper on silicon ( $\Delta\alpha$  (Cu/Si) =  $1.30 \times 10^{-5}$  per  $^{\circ}\text{C}$ )

$\Delta T$ ( $^{\circ}\text{C}$ )	$\Delta\epsilon$ (Al/Si) (%)	$\Delta\epsilon$ (Cu/Si) (%)
400	0.82	0.52
350	0.72	0.46
300	0.62	0.39
250	0.51	0.33
200	0.41	0.26
150	0.31	0.20
100	0.21	0.13
50	0.10	0.07

In a typical laboratory setup, current can usually be sufficiently well controlled without the need for highly specialized electronic equipment, to enable applied temperature amplitudes that are repeatable to approximately  $\pm 1^{\circ}\text{C}$ . This suggests control over total strain amplitude down to the range 0.001–0.002%. These ranges of temperature and strain are sufficient for characterizing the types of thermal cycling undergone by microelectronic devices during manufacture and use. Table 12.2 shows some relationships between temperature amplitude and total strain amplitude for fatigue testing of aluminum films on silicon and copper films on silicon.

With strain control down to  $10^{-5}$  and frequencies of up to several kilohertz, AC stressing also enables the study of ultra-high-cycle fatigue behavior. For example, a test running at an AC frequency of 5 kHz can result in application of  $10^{10}$  cycles in about 11.5 days. The facts that numerous test specimens can reside on one wafer, and wire-bonding methods can be used to control each specimen, point out another advantage of this test method – a large number of tests can be run in a relatively short period, so that statistically significant lifetime data can be generated much more quickly, compared to serial testing of individual specimens at lower frequencies. Furthermore, this approach to thermal fatigue testing is much faster than methods such as wafer curvature measurements associated with temperature cycling within a furnace.

Examples of microstructural changes observed in electrically cycled patterned metal interconnects will be covered in a later section, with emphases on grain structure and defect behavior. It will be shown that the damage induced by this test method does indeed take place by cyclic deformation mechanisms.

### 12.5.3 Strength Measurement

Cyclic joule heating can also be used to evaluate ultimate strength of patterned materials on substrates [81]. Predictions of fatigue lifetime from measurements of tensile properties have been made in numerous engineering materials through application

of a method termed the modified universal slopes equation, which was the result of an empirical correlation study of the fatigue lifetime behaviors of 50 steels, aluminum, and titanium alloys [82]. This strain-based approach to fatigue analysis represents total strain range,  $\Delta\varepsilon$ , as a sum of power-law terms in the elastic and plastic strain ranges

$$\frac{\Delta\varepsilon}{2} = \left(\frac{\sigma_f}{E}\right)(2N_f)^b + \varepsilon_f(2N_f)^c, \quad (12.8)$$

where  $\sigma_f$  is the true fracture strength,  $E$  is Young's modulus,  $N_f$  is the number of cycles to failure,  $\varepsilon_f$  is the true fracture strain, and  $b$  and  $c$  are fitting constants. Assumption of globally elastic behavior in each cycle, reasonable for the types of strains that microelectronic devices typically undergo, leads to

$$\frac{\Delta\varepsilon}{2} = \left(\frac{\sigma_f}{E}\right)(2N_f)^b. \quad (12.9)$$

Multiplying through by  $E$  gives a stress representation, also termed the Basquin relation

$$\Delta\sigma = \sigma_f(2N_f)^b, \quad (12.10)$$

where  $\Delta\sigma$  is the stress amplitude,  $\sigma_f$  is termed the fatigue strength coefficient in this relation, and  $b$  the fatigue strength exponent. Ultimate strength provides a reasonable estimate of  $\sigma_f$  for negligible necking [83]. Tensile data obtained from numerous materials were used to generate fatigue lifetime predictions, and those predictions compared to experimental fatigue data from the same materials [84]. Eighty percent of the fatigue data came within a factor of 3 of the predicted lifetime, which suggests that tensile data can indeed be used to reasonably predict cyclic behavior.

An inverse approach can also be taken – strength may be estimated from fatigue data such as that generated by the AC stressing method. A plot of stress amplitude vs. cycles to failure can be fit to the Basquin relation. Extrapolating such a fit to a single load reversal ( $N_f = 1/2$ ) leads to  $\Delta\sigma = \sigma_f$ , and the stress amplitude becomes equal to the ultimate strength, providing the basis for estimating strength from electrically induced fatigue data.

The electrical method of inducing cyclic strain, in the absence of controlled substrate temperature, requires additional considerations due to the fact that it imparts a nonzero mean stress to the tested material. Mean stress must be taken into consideration when applying the Basquin relation, since a tensile mean stress is observed to reduce cyclic lifetime. Morrow [85] has suggested the following modification to the Basquin relation, to properly consider the effect of mean stress,  $\sigma_m$ :

$$\Delta\sigma = (\sigma_f - \sigma_m)(2N_f)^b. \quad (12.11)$$

A log plot of stress amplitude vs. cycles to failure provides values for  $\sigma_f - \sigma_m$  and  $b$ . In the absence of control of substrate temperature, fatigue testing by cyclic Joule heating inherently causes not only a nonzero mean stress, but also a nonconstant

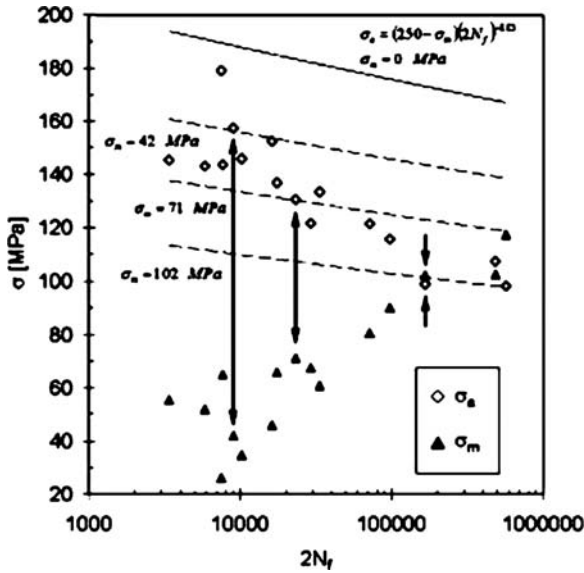


**Fig. 12.16** Stress–lifetime analysis for pure aluminum interconnects subjected to electrically induced fatigue testing. *Arrows* represent correlations between stress amplitude and mean stress for each measurement.  $\sigma_a$  is stress amplitude and  $\sigma_m$  is mean stress

mean stress. In other words, the nonzero mean stress varies with applied stress amplitude. This is a result of the fact that thermal strains are added to the initial state of residual strain in the specimen. For the case of physical-vapor-deposited metals, the residual strain tends to be tensile, so that application of additional heat acts to reduce this tensile stress, resulting in a tensile mean stress. Higher current density increases stress amplitude, but decreases the mean tensile stress.

Figure 12.16 shows a plot of stress vs. lifetime for pure aluminum interconnects subjected to AC stressing, including results of a nonlinear regression used to determine the fatigue strength coefficient and exponent [81]. The solid line represents the case for zero mean stress, and the dashed lines represent cases for tensile mean stresses of 42 MPa, 71 MPa, and 102 MPa, determined by subtracting the stress corresponding to the measured temperature amplitude from the initial level of residual stress. The open symbols are applied stress amplitude, and the filled symbols are mean stress associated with each value of stress amplitude. The regression technique for this set of aluminum interconnects resulted in a fatigue strength coefficient ( $\sim$ ultimate strength) of  $250 \pm 40$  MPa and a fatigue strength exponent of  $-0.03 \pm 0.02$ . This estimate of ultimate strength compares nicely with the value of  $239 \pm 4$  MPa obtained from microtensile specimens fabricated from the same films.

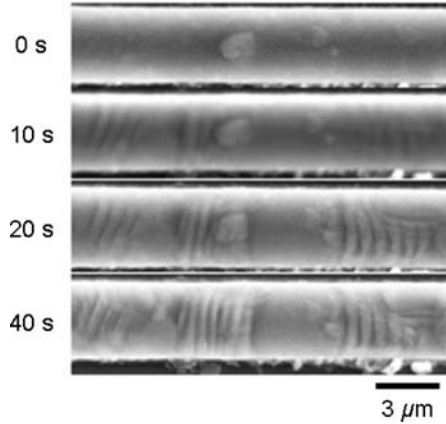
### 12.5.4 Microstructure Changes During AC Stressing

Electron-microscopic observations of the evolution of damage in aluminum and copper films subjected to cyclic Joule heating by alternating current have revealed heterogeneous behavior typical of plastic deformation in polycrystalline metals. For example, surface roughness was observed to increase with increasing cycling, but developed only in selected regions of stressed lines. The evolution of damage also included selective changes in grain size and crystallographic texture, which can be explained in terms of crystal plasticity.

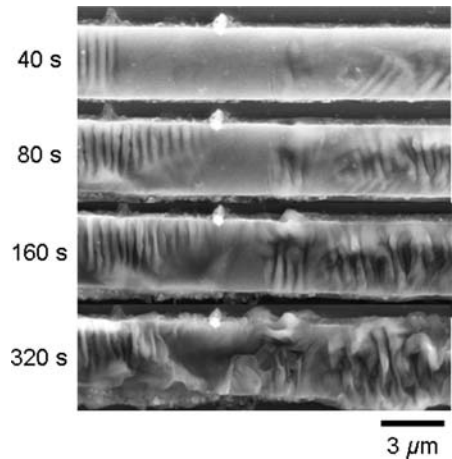
Figure 12.17 shows a sequence of SEM images taken in plan-view from one area of one specimen after it was subjected to 0 s, 10 s, 20 s, and 40 s of thermal cycling. Note the progressive development of damage, observable after even just several seconds of cycling, taking the form of surface undulations in selected areas.

Continued cycling led to the formation of severe surface topography that eventually caused open-circuit failure. Figure 12.18 shows a sequence of SEM images that

**Fig. 12.17** SEM sequence showing development of surface topography in selected regions of an Al–1Si interconnect subjected to the indicated levels of accumulated cycling. Current density of  $12.2 \text{ MA cm}^{-2}$ , cyclic straining frequency of 200 Hz



**Fig. 12.18** SEM sequence showing advanced stages of surface damage in a different region of same specimen as that shown in Fig. 12.17



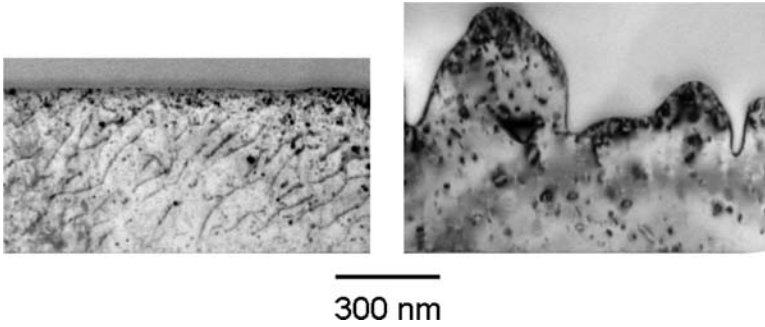


**Fig. 12.19** TEM images showing variations in surface topography from one region to another, after  $1.39 \times 10^5$  thermal cycles, or 697 s of cycling, within the same specimen of Al-1Si shown in Figs. 12.17 and 12.18. The images also show differences in dislocation arrangements, with the image on the *left* containing more isolated dislocation segments and fewer dislocation loops than the image on the *right*. The *bottom edge* of both images corresponds to the substrate surface

demonstrate more advanced degrees of damage in the same specimen; the particular specimen under observation failed after 697 s of thermal cycling. Cross-sectional TEM observations showed that the surface topography that developed as a result of thermal cycling varied considerably from place to place within one specimen, as shown in Fig. 12.19, corresponding to natural variations in localized plasticity from grain to grain [86]. Both grains shown in the figure were part of a specimen cycled for  $1.39 \times 10^5$  thermal cycles. The grain in the left image of the figure shows a flat surface, virtually unchanged from its original thickness of  $0.5 \mu\text{m}$ . Surface upsets corresponding to a local film thickness of approximately  $0.7 \mu\text{m}$  and depressions corresponding to a local film thickness of approximately  $0.3 \mu\text{m}$  are visible in the grain shown in the right image of the figure. Figure 12.19 also shows the presence of dislocations in the film – the grain with a flatter surface contains residual dislocation segments, while the grain with surface undulations is free of isolated segments, but contains debris in the form of prismatic loops. In the latter case, dislocations could easily glide and leave the surface, resulting in upsets and depressions akin to intrusions and extrusions seen in purely mechanical fatigue; prismatic loop debris is typically left behind in face-centered cubic metals as a result of extensive dislocation glide [87]. In the case of the flatter surface, residual segments remained in the interior of the grain due to localized variations in grain size, dislocation sources, or resolved shear stress, any of which could inhibit dislocation motion.

Mapping of the grain structure by automated electron backscatter diffraction (EBSD) showed that with increased cycling, some grains grew considerably, while others disappeared [86]. An example is shown in Fig. 12.20, where after just 2,000 thermal cycles, grain “A” increased in area by 114%, representing an equivalent circular diameter increase from  $3.0$  to  $4.4 \mu\text{m}$ . Grain “B” shows an area increase of 60%, corresponding to an equivalent circular diameter increase from  $4.0$  to  $5.2 \mu\text{m}$ .

Measurements made over a  $100 \mu\text{m} \times 3 \mu\text{m}$  region of the tested interconnect showed that the mean grain diameter increased from  $1.4 \pm 0.4 \mu\text{m}$  at the start of the

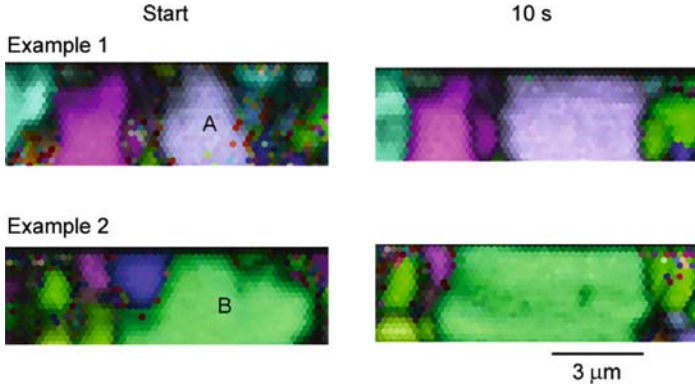


**Fig. 12.20** EBSD maps showing two examples of grain growth in an Al–Si interconnect subjected to 2,000 thermal cycles at 200 Hz. *Left images* represent grains at start of test; *right images* represent grains after cycling

test to  $2.4 \pm 0.4 \mu\text{m}$  after  $6.4 \times 10^4$  thermal cycles. Correlations of residual dislocation content with EBSD pattern sharpness [86] showed that grains that grew tended to be those that had lower residual dislocation content. Grains that shrank tended to be those that had higher residual dislocation content. This set of observations suggested that during rapid thermal cycling as induced by alternating current, grain growth takes place by strain-induced boundary migration [88, 89], wherein stored plastic strain energy differences from grain to grain drive growth.

### 12.6 Summary and Outlook

In a discussion of metrologies developed at NIST for determination of mechanical response of micro- and nanoscale systems, we have addressed three emerging approaches. First, we discussed new tools to measure and image mechanical properties that exploit the nanoscale spatial resolution of the atomic force microscope. Contact-resonance AFM methods examine the resonant modes of a vibrating AFM cantilever when its tip is in contact with a specimen. The frequency information is used to deduce the tip–sample contact stiffness, from which near-surface properties such as local elastic modulus can be extracted. In addition to the basic physical principles involved, the experimental apparatus and measurement methods were discussed. Examples were also given of the different information that can be obtained with contact-resonance AFM methods. This includes not only measurements of the indentation modulus  $M$  at a single sample location, but also elastic-property imaging and mapping, and evaluating thin-film adhesion at a buried interface. The results discussed here, as well as those from groups around the world, show significant progress in advancing the state of the art. It is anticipated that contact-resonance AFM techniques will continue to develop, and will play a significant role in future nanotechnology efforts by providing quantitative nanomechanical information.

In regard to microtensile testing for direct determination of film properties, the practical issue facing experimentalists now is the need for imaging at magnifications higher than optical microscopy can provide. The logical path forward would be to test routinely within the SEM or TEM. Haque et al. [59] have shown one possible path, but it requires a big advance in specimen fabrication over the one-mask, micrometer-scale lithography that suffices for specimens for testing under the optical microscope.

Scientific impetus for additional advances in mechanical test techniques may come from a new frontier of materials research – mechanical behavior of small volumes of material. The effects of “length scale” on mechanical behavior have received intense study recently [90]. A complementary viewpoint is that fine-scale microstructural variation may become significant when an experiment samples the behavior of materials of very small volumes, for example, the material under the sharp tip of a nanoindenter [91]. Tensile testing of *films* has not contributed any of the surprising results in this new field, but eventually the question of whether and when small volume effects appear in the behavior of tensile specimens will have to be answered.

The ultimate length scale for mechanical property measurements is the few-atom scale, which may be a source of insight into the behavior of practical materials, and may also be important in establishing the accuracy of atomistic modeling approaches such as molecular dynamics. In this regard, the results reported by Rubio-Bollinger et al. [92], which seem to show that a chain of gold atoms can have a strength value (calculated by the authors from the results in [92]) surpassing that of high-strength steel, stand as a challenge to material testers and material developers alike. Another provocative recent result by Uchic et al. [93] seems to show that small volume effects can begin to appear in stressed cross sections with an area of hundreds of square micrometers. At the present time this result seems to be at odds with the typical results of microtensile testing of specimens with the typical  $1 \times 10 \mu\text{m}^2$  cross section, because the tensile results are generally considered to be consistent with the behavior of the bulk material when the Hall–Petch rule is used to account for the grain size.

Extending our test methodologies to approaches that do not require special specimen configurations, we have presented a method for inducing thermal fatigue in patterned thin films on substrates, by application of alternating current under conditions of low frequency and high current density. The sole requirement is that the specimen be accessible electrically. The AC stressing method makes use of differences in coefficients of thermal expansion between the test film of interest and its substrate. Measurements of fatigue lifetime are straightforward with this approach, when coupling the raw data with calibration of specimen resistance with temperature. Ultimate strength can also be measured, by extrapolation of fatigue data back to a single load reversal. At this point, the electrical approach is still under development, but holds promise for accessing the mechanical response of extremely narrow structures, unusual geometries, and films buried beneath other layers, all of which pose significant difficulties for the more established methods for measuring mechanical response.

**Acknowledgments** The contributions of current and former NIST coworkers (R. Geiss, M. Kopycinska-Müller, and E. Langlois) are gratefully acknowledged. We also value interactions with the research groups of J. Turner (Univ. Nebraska–Lincoln) and W. Arnold and U. Rabe (Fraunhofer Institut für Zerörungsfreie Prüfverfahren, Saarbrücken, Germany). Nanoindentation measurements for comparison to contact-resonance AFM results were provided by N. Jennett (National Physical Laboratory, UK), A. Rar (then at Univ. Tennessee–Knoxville), and D. Smith (NIST). We thank E. Arzt (Max-Planck-Institute for Metals Research, Stuttgart, Germany), C. Volkert (Univ. Göttingen, Germany), and R. Mönig (Forschungszentrum Karlsruhe, Germany) for fruitful collaborations on development of electrical test methods for thermal fatigue. We are grateful for support from the NIST Office of Microelectronics Programs.

## References

1. Binnig G, Quate CF, Gerber Ch (1986) *Phys. Rev. Lett.* 56:930
2. Maivald P, Butt HJ, Gould SAC, Prater CB, Drake B, Gurley JA, Elings VB, Hansma PK (1991) *Nanotechnology* 2:103
3. Burnham NA, Kulik AJ, Gremaud G, Gallo PJ, Oulevey F (1996) *J. Vac. Sci. Technol. B* 14:794
4. Troyon M, Wang Z, Pastre D, Lei HN, Hazotte A (1997) *Nanotechnology* 8:163
5. Rosa-Zeiser A, Weilandt E, Hild S, Marti O (1997) *Meas. Sci. Technol.* 8:1333
6. Butt HJ, Cappella B, Kappl M (2005) *Surf. Sci. Rep.* 59:1
7. Zhong Q, Inniss D, Kjoller K, Elings VB (1993) *Surf. Sci.* 290:L688
8. Yamanaka K, Ogiso H, Kolosov OV (1994) *Appl. Phys. Lett.* 64:178
9. Cuberes MT, Assender HE, Briggs GAD, Kolosov OV (2000) *J. Phys. D: Appl. Phys.* 33:2347
10. Yamanaka K, Nakano S (1996) *Jpn. J. Appl. Phys.* 35:3787
11. Rabe U, Arnold W (1994) *Appl. Phys. Lett.* 64:149
12. Yamanaka K, Nakano S (1998) *Appl. Phys. A* 66:S31
13. Crozier KB, Yaralioglu GG, Degertekin FL, Adams JD, Minne SC, Quate CF (2000) *Appl. Phys. Lett.* 76:195
14. Hurley DC, Shen K, Jennett NM, Turner JA (2003) *J. Appl. Phys.* 94:2347
15. Rabe U (2006) In: Bushan B, Fuchs H (eds) *Applied Scanning Probe Methods*, vol. II. Springer, New York, chap. 2
16. Huey BD (2007) *Annu. Rev. Mater. Res.* 37:351
17. Rabe U, Amelio S, Kester E, Scherer V, Hirsekorn S, Arnold W (2000) *Ultrasonics* 38:430
18. Arinero R, Lévêque G (2003) *Rev. Sci. Instrum.* 74:104
19. Johnson KL (1985) *Contact Mechanics*. Cambridge University Press, Cambridge, UK
20. Vlassak JJ, Nix WD (1993) *Philos. Mag. A* 67:1045
21. Rabe U, Amelio S, Kopycinska M, Hirsekorn S, Kempf M, Göken M, Arnold W (2002) *Surf. Interface Anal.* 33:65
22. Kopycinska-Müller M, Geiss RH, Hurley DC (2006) *Ultramicroscopy* 106:466
23. Yamanaka K, Tsuji T, Noguchi A, Koike T, Mihara T (2000) *Rev. Sci. Instrum.* 71:2403
24. Prasad M, Kopycinska M, Rabe U, Arnold W (2002) *Geophys. Res. Lett.* 29:13
25. Stan G, Price W (2006) *Rev. Sci. Instrum.* 77:103707
26. Hurley DC, Kopycinska-Müller M, Kos AB, Geiss RH (2005) *Meas. Sci. Technol.* 16:2167
27. Rabe U, Amelio S, Kopycinska M, Hirsekorn S, Kempf M, Göken M, Arnold W (2002) *Surf. Interface Anal.* 33:65
28. Passeri D, Bettucci A, Germano M, Rossi M, Alippi A, Orlanducci S, Terranova ML, Ciavarella M (2005) *Rev. Sci. Instrum.* 76:093904
29. Zheng Y, Geer RE, Dovidenko K, Kopycinska-Müller M, Hurley DC (2006) *J. Appl. Phys.* 100:124308

30. Stan G, Ciobanu CV, Parthangal PM, Cook RF (2007) *Nano Lett.* 7(12):3691
31. Kopycinska-Müller M, Geiss RH, Müller J, Hurley DC (2005) *Nanotechnology* 16:703
32. Hurley DC, Turner JA (2007) *J. Appl. Phys.* 102:033509
33. Rabe U, Kopycinska M, Hirsekorn S, Muñoz Saldaña J, Schneider GA, Arnold W (2002) *J. Phys. D: Appl. Phys.* 35:2621
34. Tsuji T, Yamanaka K (2001) *Nanotechnology* 12:301
35. Yamanaka K, Maruyama Y, Tsuji T, Nakamoto K (2001) *Appl. Phys. Lett.* 78:1939
36. Passeri D, Bettucci A, Germano M, Rossi M, Alippi A, Sessa V, Fiori A, Tamburri E, Terranova ML (2006) *Appl. Phys. Lett.* 88:121910
37. Kos AB, Hurley DC (2008) *Meas. Sci. Technol.* 19:015504
38. Hurley DC, Kopycinska-Müller M, Langlois ED, Kos AB, Barbosa N (2006) *Appl. Phys. Lett.* 89:021911
39. Sarioglu AF, Atalar A, Degertekin FL (2004) *Appl. Phys. Lett.* 84:5368
40. Read DT, Dally JW (1993) *J. Mater. Res.* 8:1542
41. Cheng YW, Read DT, McColskey JD, Wright JE (2005) *Thin Solid Films* 484:426
42. Read DT, Volinsky AA (2007) In: Suhir E, Lee YC, Wong CP (eds) *Materials and Structures: Physics, Mechanics, Design, Reliability, Packaging: Volume 1. Materials Physics / Materials Mechanics.* Springer, New York, chap. 4, pp. 135–180
43. Dieter G (1986) *Mechanical Metallurgy.* McGraw-Hill, New York
44. Hoffman RW (1989) In: Bravman JC, Nix WD, Barnett DM, Smith DA (eds) *Mater. Res. Soc. Symp. Proc.*, vol. 130. Materials Research Society, Warrendale, pp. 295–306
45. Brotzen FR (1994) *Int. Mater. Rev.* 39:24
46. ASTM (2004) E8-04 Standard Test Methods for Tension Testing of Metallic Materials. American Society for Testing and Materials, West Conshohocken, PA
47. ASTM (2004) E345-93(2002) Standard Test Methods of Tension Testing of Metallic Foil. American Society for Testing and Materials, West Conshohocken, PA
48. Hoffman RW (1966) In: Hass G, Thun RE (eds) *Physics of Thin Films.* Academic, New York, pp. 211–273
49. Menter JW, Pashley DW (2007) In: Neugebauer CA, Newkirk JB, Vermilyea DA (eds) *Structure and Properties of Thin Films.* Wiley, New York, pp. 111–148
50. Ding XY, Ko WH, Mansour JM (1990) *Sens. Actuators A Phys.* 23:866
51. Ruud JA, Josell D, Spaepen F, Greer AL (1993) *J. Mater. Res.* 8:112
52. Steinwall JE (1994) Ph.D. thesis, Cornell University, Ithaca, NY
53. Sharpe WN, Yuan B, Edwards RL (1997) *J. Microelectromech. Syst.* 6:193
54. Read DT (1998) *J. Test. Eval.* 26:255
55. Read DT, Dally JW (1995) *J. Electron. Packaging* 117:1
56. Read DT (1998) *Int. J. Fatigue* 20:203
57. Read DT (1998) *Meas. Sci. Technol.* 9:676
58. Fox JC, Edwards RL, Sharpe WN (1999) *Exp. Tech.* 23:28
59. Haque MA, Saif TA (2004) *Proc. Natl. Acad. Sci. USA* 101:6335
60. Espinosa HD, Prorok BD, Peng B (2004) *J. Mech. Phys. Solids* 52:667
61. Read DT, Cheng YW, Keller RR, McColskey JD (2001) *Ser. Mater.* 45:583
62. Bruck HA, McNeill SR, Sutton MA, Peters WH (1989) *Exp. Mech.* 29:261
63. Read DT, Cheng YW, Sutton MA, McNeill SR, Schreier H (2001) In: Shukla A, O'Brien EW, French RM, Ramsay KM (eds) *Proceedings of the SEM Annual Conference and Exposition on Experimental and Applied Mechanics.* Society for Experimental Mechanics, Bethel, CT, pp. 365–368
64. Read DT, Cheng YW, Geiss R (2004) *Microelectron. Eng.* 75:63
65. Read DT, Cheng YW, McColskey JD (2002) In: *Proceedings of the SEM Annual Conference and Exposition on Experimental and Applied Mechanics.* Society for Experimental Mechanics, Bethel, CT, pp. 64–67
66. Hurley DC, Geiss RH, Kopycinska-Müller M, Müller J, Read DT, Wright JE, Jennett NM, Maxwell AS (2005) *J. Mater. Res.* 20:1186

67. LaVan DA, Tsuchiya T, Coles G, Knauss WG, Chasiotis I, Read DT (2001) In: Muhlstein C, Brown SB (eds) ASTM STP 1413: Mechanical Properties of Structural Films. American Society for Testing and Materials, West Conshohoken, PA, pp. 16–27
68. Espinosa HD, Prorok BC, Peng B (2004) *J. Mech. Phys. Solids* 52:667
69. Haque MA, Saif TA (2002) In: Shukla A, French RM, Andonian A, Ramsey K (eds) SEM Annual Conference and Exposition on Experimental and Applied Mechanics. Society of Experimental Mechanics, Bethel, CT, pp. 134–138
70. Read DT, Cheng YW, McColskey JD, Keller RR (2002) In: Ozkan CS, Freund LB, Cammarata RC, Gao H (eds) *Mater. Res. Soc. Symp. Proc.*, vol. 695. Materials Research Society, Warrendale, PA, pp. 263–268
71. Read DT, Geiss R, Ramsey J, Scherban T, Xu G, Blaine J, Miner B, Emery RD (2003) In: Bahr DF (ed) *Mater. Res. Soc. Symp. Proc.*, vol. 778. Materials Research Society, Warrendale, PA, pp. 93–98
72. Yeung B, Lytle W, Sarihan V, Read DT, Guo Y (2002) *Solid State Technol.* 45(6):125
73. Sharpe WN, Jackson KM, Coles G, Eby MA, Edwards RL (2001) In: Muhlstein C, Brown SB (eds) ASTM STP 1413: Mechanical Properties of Structural Films. American Society for Testing and Materials, West Conshohoken, PA, pp. 229–247
74. Read DT, Keller RR, Barbosa N, Geiss R (2007) *Metall. Mater. Trans. A* 38A:2242
75. Philofsky E, Ravi K, Hall E, Black J (1971) In: *Proc. 9th Annual Reliability Physics Symposium*. IEEE, New York, pp. 120–128
76. Mönig R, Keller RR, Volkert CA (2004) *Rev. Sci. Instrum.* 75:4997
77. Ho PS, Kwok T (1989) *Rep. Prog. Phys.* 52:301
78. Ting LM, May JS, Hunter WR, McPherson JW (1993) In: *Proc. 31st Annual Reliability Physics Symposium*. IEEE, New York, pp. 311–316
79. Keller RR, Barbosa III N, Geiss RH, Read DT (2007) *Key Eng. Mater.* 345:1115
80. Manson SS, Halford GR (2006) *Fatigue and Durability of Structural Materials*. ASM International, Materials Park, OH, p. 64
81. Barbosa III N, Keller RR, Read DT, Geiss RH, Vinci RP (2007) *Metall. Mater. Trans.* 38A:2160
82. Muralidharan U, Manson SS (1988) *J. Eng. Mater. Technol. Trans. ASME* 110:55
83. Suresh S (1998) *Fatigue of Materials*, 2nd edn. Cambridge University Press, Cambridge, UK, p. 223
84. Nachtigall AJ (1975) *Properties of Materials for Liquefied Natural Gas Tankage*, ASTM STP 579. American Society for Testing and Materials, West Conshohocken, PA, pp. 378–396
85. Morrow JD (1968) *Fatigue Design Handbook – Advances in Engineering*. Society of Automotive Engineers, Warrendale, PA, pp. 21–29
86. Keller RR, Geiss RH, Barbosa III N, Slifka AJ, Read DT (2007) *Metall. Mater. Trans.* 38A:2263
87. Kuhlmann-Wilsdorf D, Wilsdorf HGF (1963) *Electron Microscopy and Strength of Crystals*. Interscience, New York, pp. 575–604
88. Beck PA, Sperry PR (1950) *J. Appl. Phys.* 21:150
89. Battaile CC, Buchheit TE, Holm EA, Wellman GW, Neilsen MK (1999) In: *Mater. Res. Soc. Symp. Proc.*, vol. 538. Materials Research Society, Warrendale, PA, pp. 267–273
90. Haque MA, Saif MTA (2003) *Acta Mater.* 51:3053
91. Greer JR, Oliver WC, Nix WD (2005) *Acta Mater.* 53:1821
92. Rubio-Bollinger G, Bahn SR, Agrait N, Jacobsen KW, Vieira S (2001) *Phys. Rev. Lett.* 87:026101
93. Uchic MD, Dimiduk DM, Florando JM, Nix WD (2004) *Science* 305:986